Intrinsically Strained Noble Metal-Free Oxynitrides for Solar Photoreduction of CO_2

Debtanu Maiti[1,§], Anne J. Meier[1,2,§], Johnnie Cairns[1], Swetha Ramani[3], Karen Martinet[1], John N. Kuhn[1,3,*], Venkat R. Bhethanabotla[1,3,*]

[1]Department of Chemical & Biomolecular Engineering, University of South Florida, Tampa, FL – 33620 , USA.
[2] Laboratory - Development and Testing Division, NASA Kennedy Space Center, FL – 32899. Mail Stop NE-L3, USA.
[3]Department of Chemistry, University of South Florida, Tampa, FL-33620, USA.

ABSTRACT:

Metal oxynitrides demonstrate promising activity for photocatalytic solar water splitting and CO_2 reduction under solar irradiance aided by noble metals. Precise control of cation ratios in the oxynitrides is a necessary challenge needed to overcome for achieving effective band gap tuning. Here we report density functional theory-based calculations on intricate structure-function relationships of Zn-Ga based oxynitrides and correlate results with the experimental parameters. Crucial material property descriptors such as elemental composition, intrinsic lattice strain, and vacancy defects were exploited during the synthesis to achieve stable oxynitride photocatalysts that demonstrated CO_2 conversion to CO under simulated solar spectrum, without any noble metal impregnation. The highest CO production rate surpassed that of TiO_2 under the same conditions. This work inspires future research on oxynitride materials towards tailored optical properties and sustainable photocatalytic activity enabling large scale applications.

*Email Correspondence: jnkuhn@usf.edu (JNK) and bhethana@usf.edu (VRB)
§ These authors contributed equally to this paper.

INTRODUCTION:

Solar based CO_2 conversion techniques behold the promise of reutilizing the waste CO_2 from the atmosphere towards generating high-value hydrocarbons[1, 2]. These processes allow for harvesting the abundant sunlight and is a major step towards reduction of global carbon footprint by creating a closed loop synthetic carbon cycle. Amongst many potential solar processes, photocatalysis presents the advantage of low temperature operation as opposed to solar thermochemical based process[2-5]. However, the major limitations of photocatalysis being implemented at large scale are the poor reaction rates, fast exciton recombination resulting in poor quantum efficiency, and photocatalytic activity only under UV illumination[6-10]. The reactivity of the catalysts is usually enhanced by the addition of noble metals or metal oxides like platinum, ruthenium, ruthenium oxides and so forth, thus increasing the operational costs of photocatalysis. Significant effort has been spent on exploring new materials that are visible light active and exhibit appreciable photoreduction rates without the use of noble metal co-catalysts. Recently, layered double hydroxides (LDH) and metal oxynitrides have garnered interest due to their intrinsic capability for elemental composition tuning[11, 12].

Zn-based LDH has shown promising results for photocatalysis[13, 14]. Zn-Al based LDH demonstrated CO_2 photoreduction to CO (94% selective) under UV-illumination, while Cu doped Zn-Ga based LDH produced methanol[13]. These materials are limited to UV light induced photoreduction, due to their intrinsically large band gaps[14]. Nitriding these materials towards the generation of metal oxynitrides has proved beneficial for band gap reduction. Zn-Ga and Zn-Ge based oxynitrides in particular have shown promising results for solar water and CO_2 splitting reactions[8, 15-17]. A high solar water splitting activity was achieved by Zn-Ga based oxynitride solid solutions, using noble metal co-catalysts[18]. Visible light CO_2 photoreduction was observed for Zn-

Ge oxynitrides along with Pt co-catalysts[8]. Rh and Cr nanoparticles impregnated Zn-Ge oxynitrides also demonstrated solar water splitting activity[16, 19]. Even Zn-Al modified Zn-Ga oxynitride solid solutions along with 0.5 wt% Pt produced CH_4 from CO_2 under visible light[20]. This capability of visible light harvesting is attributed to narrowing of the band gap due to the repulsion of the Zn-*3d* and N-*2p* orbitals in the valence band edge (VBE)[21-23]. Low-dimensional materials such as these provide improvement in photocatalytic efficiency[24] when paying close attention to the architecture and synthesis variables to form heterostructures for efficient charge dissociation as we have studied here both experimentally and theoretically.

Through this effort, we portray the enormous opportunity in modulating simple synthesis parameters towards improved catalytic activity. Harnessing the experimental parameters is a natural pathway towards tailored material properties, as achieved in this study via lattice strain, oxide/nitride composition and vacancy defect tuning of these materials. However, a key limitation of these oxynitride synthesis protocols is the volatilization of Zn resulting in poor Zn^{2+}/M^{3+} ratios (M being any suitable metal like Al, Ga, Ge etc.), mostly less than 0.3[20]. In the absence of appropriate control of material composition of these oxynitrides, tuning of the band gap for enhanced photocatalytic activity is hindered. A systematic study of the material chemistry during the growth of these oxynitrides is clearly indicated. Elucidating the electronic structure-function relationships in these materials and their close correlation to the experimental synthesis parameters is thus of extreme importance. Although several studies have tried to improve the synthesis protocol through modification of the nitriding techniques[25-27], none of them yet has reported solar CO_2 photoreduction over these oxynitrides, without the use of noble metals. We hereby explore the effects of intrinsic structural parameters like composition, strain, vacancy, lattice spacing towards electronic band gap modulation of Zn-Ga oxynitrides. We developed a profound

understanding of the oxynitride solid solution as a function of the synthesis parameters. Solar CO_2 photoreduction to CO without the use of any noble metal based co-catalysts is shown for the first time with these materials.

MATERIALS AND METHODS:

Experimental methodology:

The Zn-Ga oxynitride solid solutions were prepared using a co-precipitation method that involved Zn-Ga-CO_3 LDH precursor synthesis followed by nitridation as reported in literature[28]. The LDHs were prepared by mixing the precursor materials to form a precipitate that contained the carbonate interlayer anions. For production of the Zn-Ga-CO_3, stoichiometric amounts of $Zn(NO_3)_2{\cdot}6H_2O$ (98% purity, Sigma-Aldrich) and $Ga(NO_3)_3{\cdot}9H_2O$ (99.9% purity with trace metals basis, Sigma-Aldrich) were mixed in deionized (DI) water and dissolved completely. Separately, Na_2CO_3 (≥99.5% purity, Fisher) was dissolved in DI H_2O. The nitrate solution was then slowly added dropwise to 74.5 mL of a 1 M Na_2CO_3 solution, forming the LDH precipitate. Nitridation of the LDH materials was done in a combustion dish at a ramp rate of 5 °C/min to 800 °C in a tube furnace (Thermo Scientific Lindberg/Blue M) with a constant NH_3 gas flow rate of 300 sccm.

The crystallinity of the samples were probed via x-ray powder diffraction (PXRD) obtained using a PANanalytical Empyrean machine with Cu Kα radiation (λ = 0.15406 nm) at a scan rate (2θ) of 0.02 degrees per sec. In-situ XRD experiments were performed with a PANalytical X'Pert Pro with an XRK-900 accessory at 1000 mbar (~1 atm) and 10°C/min ramp from 25 to 200°C in CO_2 and air. The oxygen and nitrogen content of solids were measured using a LECO TC 600 elemental analyzer according to the "Oxygen and Nitrogen in Nitride Material" method. Imaging and elemental analysis were obtained using SEM-EDS (JEOL JSM-7500F field emission SEM

(FESEM), and Hitachi S800 scanning electron microscopy (SEM) with Phoenix energy-dispersive X-ray spectroscopy (EDS)). Zinc and gallium content in the samples were obtained from EDS. A Tecnai F20 TEM with a line resolution of 0.102 nm was used to acquire the morphology and *d* spacing of the exposed lattice plane. Optical absorption properties were analyzed using a Jasco V-760 UV-visible (UV/Vis) spectrophotometer equipped with an ISN-723 Integrating Sphere to obtain diffuse reflectance spectroscopy (DRS). Raman spectroscopy data was collected with a Thermo Scientific DXR2 Raman Microscope at 10x, with a high resolution DXR 532 nm laser. The laser power was 6 mW and the aperture was a 50 μm pinhole with a 900 line/cm gratin and 2.1 μm spot size. The resolution was 5.5-8.3 cm^{-1}. X-ray photoelectron spectrometry (XPS) measurements were conducted with a Thermo Scientific K-Alpha instrument using Al Kα radiation. The samples were prepared in air for XPS measurements and the scans were collected for the nitrided powders before and after UV exposure (F15T8 bulbs at 75 W/m^2) to determine stability with a C *1s* binding energy reported at 285.3 eV.

Diffuse Reflectance Infrared Fourier Transform spectroscopy (DRIFTS) was done to probe the CO_2 adsorption properties of the samples. A Harrick high temperature-high pressure reactor cell along with Nicolet IS50 spectrometer from Thermo Scientific was used for the purpose. The samples were loaded in the cell along with water addition. The cell was purged off any ambient gases by flowing pure argon (AIRGAS, UHP-300, 50 sccm) for 60 min at 50 °C. Carbon dioxide (AIRGAS, UN1013, 20 sccm) flowed subsequently over the samples for 15 min. Excess CO_2 was purged off by flowing Ar. A temperature-programmed desorption (TPD) study was thereafter ensued with a ramp rate of 10 °C/min from 50 to 300 °C. 250 scans were recorded for each TPD spectrum with a resolution of 0.241 cm^{-1}.

The photocatalytic reactions took place in a chemically resistant stainless steel rectangular reactor cell in a network of fluid lines and analytical instrumentation with a total fluid volume of approximately 73 cm^3. Evolved gases were separated and analyzed with an IonCam 2020 gas chromatograph (GC) and mass spectrometer (MS) system, equipped with a thermal conductivity detector (SRA Instruments with 99.9999% He carrier gas and Plot Q GC column). The light source used for the photoreduction experiments was a 1600 W Xe arc lamp (1400 W) equipped with a lamp housing (Newport 66870 housing with 3177 heat sink and 69922 power supply), aluminum liquid filter (Newport 6123NS, 2 inch), a quick change filter holder (Newport 71260) and a fiber bundle focusing assembly (Newport 77776). The H_2O filter limited the lamp output range to approximately 280-950 nm. A Newport AM0 filter was used in the quick change filter. A LI-COR LI-200R Pyranometer with a LI-250A light meter was used to measure the global solar radiation output of the solar simulator. The light output measured directly onto the region of catalyst after equipment pass through was measured at 589 W/m^2 for the 400-700 nm range for all experiments.

Computational methodology:

Zn-Ga oxynitride solid solutions were probed computationally by spin-polarized density functional theory (DFT) calculations with plane wave basis sets using Vienna Ab initio simulation package (VASP-5.3.3). Throughout most of the calculations, the projector augmented wave (PAW) based potentials and Perdew-Burke-Ernzerhof (PBE) exchange-correlations were used. For the band-gap calculations, along with PBE, HSE06 and GW methods were used as well. The wurtzite phases of oxynitride structures were made of supercells consisting of 32, 48 or 64 atoms based on the composition. A Gamma-centric 8×8×8 *k*-point mesh was used for the 32 atom supercells. For larger systems (48 and 64 atoms) the *k*-point grid was varied accordingly to

maintain similar *k* spacing. The strained structures were created by expanding or compressing the lattice constants. The percentage strain induced in the system was calculated as:

$\frac{100\times(c_f-c_i)}{c_i}$ (for vertical strain) and $\frac{100\times(a_f-a_i)}{a_i}$, $\frac{100\times(b_f-b_i)}{b}$ (for biaxial strain), where, a, b, and c are the respective lattice constants while *f* and *i* represent the final and initial states of the material.

RESULTS AND DISCUSSIONS:

Zn-Ga based oxynitrides were synthesized by a two-step co-precipitation and nitriding process. The co-precipitation process yields the layered double hydroxide (LDH) samples, as indicated in their respective X-ray diffraction patterns (Fig. 1A). They are labeled (Table S1) as per the initial Zn:Ga precursor ratios (1 stands for 1:1, 2 stands for 2:1, and 3 stands for 3:1).Subsequently, these were nitrided for varying times (10, 20, and 30 min) under NH_3 flow at a temperature of 700 °C. The samples were labeled as precursor ratio-nitriding time (eg. 2-20 stands for Zn:Ga=2:1 precursor nitrided for 20 min). Powder X-ray diffraction patterns for these nitrided samples (Fig. 1B) closely match with the hexagonal wurtzite phase. Samples with higher Zn:Ga precursor ratios (2:1 and 3:1) favored better crystallinity as compared to Zn:Ga=1:1. The effect of the precursor composition in these oxynitrides is detailed in Fig. 1C. Increasing the ZnO fraction results in the crystal structure aligning more with that of ZnO (ZnO position marked by the black vertical lines; and that for GaN marked by red lines). Left shift of the positions, representing the increased *d* spacing to account for more ZnO content, with increasing ZnO composition is consistent for all lines except (002). For the *hkl* plane (002), the position shifted further left than that of ZnO, a pattern consistent with all the three compositions. This marks the presence of strained phases, along the *c* axis. Being generated from LDH type structures, it is quite rational to have oxynitride phases with expanded *c* lattice. This result is corroborated from our microscopy and spectroscopy studies as well (detailed later). With increasing nitriding time (Fig. 1D-E), the

right shift is coherent with the decreased cell volume due to Zn volatilization. While the shift is prominent in Zn:Ga=1:1 sample, Zn:Ga=2:1 and Zn:Ga = 3:1 exhibited almost no variation. Cell volume of Zn:Ga=1:1 sample collapsed the most which is attributed to the inherently lower crystallinity of the Ga-rich samples as opposed to the Zn-rich samples.

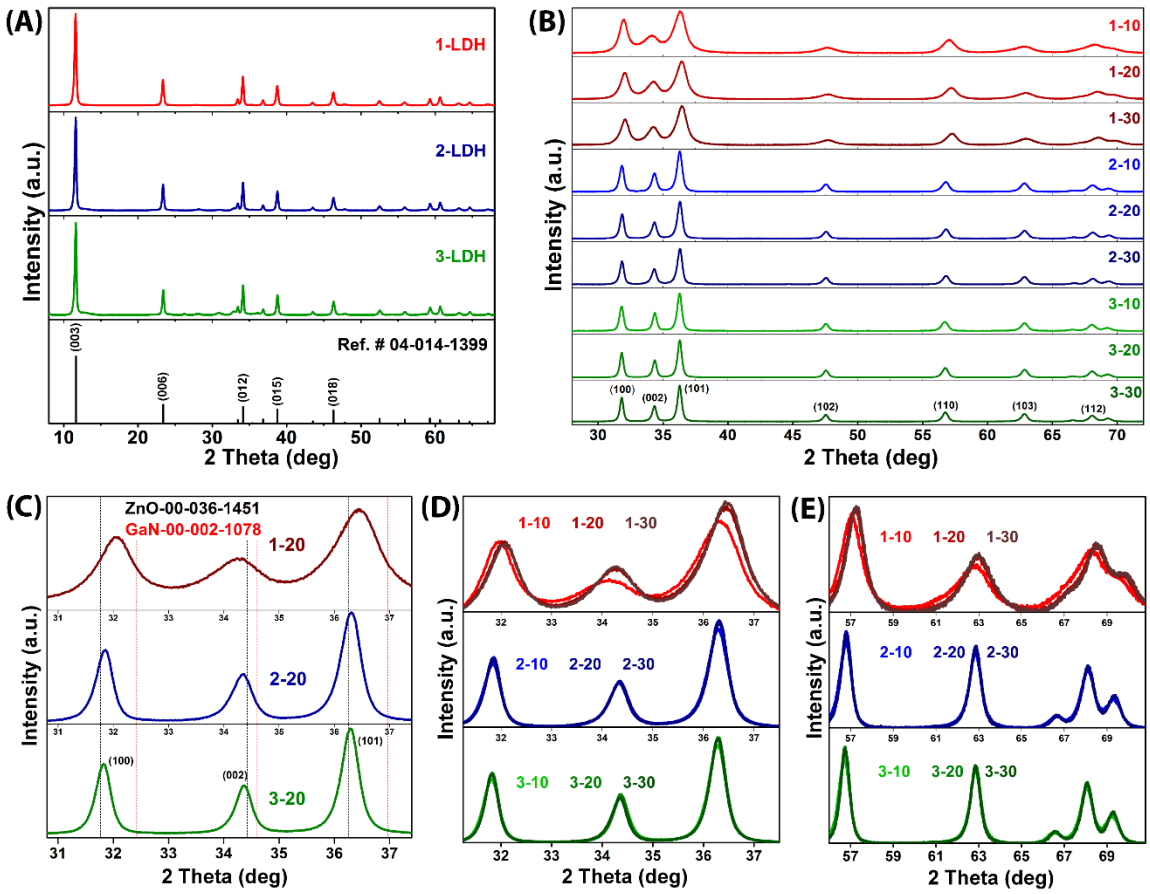

Fig. 1 | Crystal structure tuning of LDH and Oxynitrides. A, PXRD patterns of LDH samples. **B,** PXRD patterns of oxynitride samples, as obtained by nitriding the LDH for varying times. **C,** Comparison of the PXRD positions with the reference patterns for wurtzite phase ZnO and GaN. **D-E,** Shift of the positions of different oxynitrides with varying nitriding times.

SEM and TEM images along with elemental mapping via EDS are presented in Fig. 2. The SEM images (Fig. 2A-B) for the 3-20 sample shows disk shaped nanostructures, while the EDS maps (Fig. 2C-F) reveal a uniform distribution of the elements throughout the sample, as is

expected for a bulk oxynitride solid solution. The TEM images for 1-20, 2-20 and 3-20 samples (Fig. 2G-I, respectively) reveal the approximate particle size within 50-200 nm. The HRTEM images of these samples exhibit the presence of (002) crystal facets. The *d* spacings of these planes are around 0.26 nm (~0.258 nm for ZnO), indicating the presence of vertical tensile strain inherent in these materials, as was expected from the PXRD patterns in Fig. 1C.

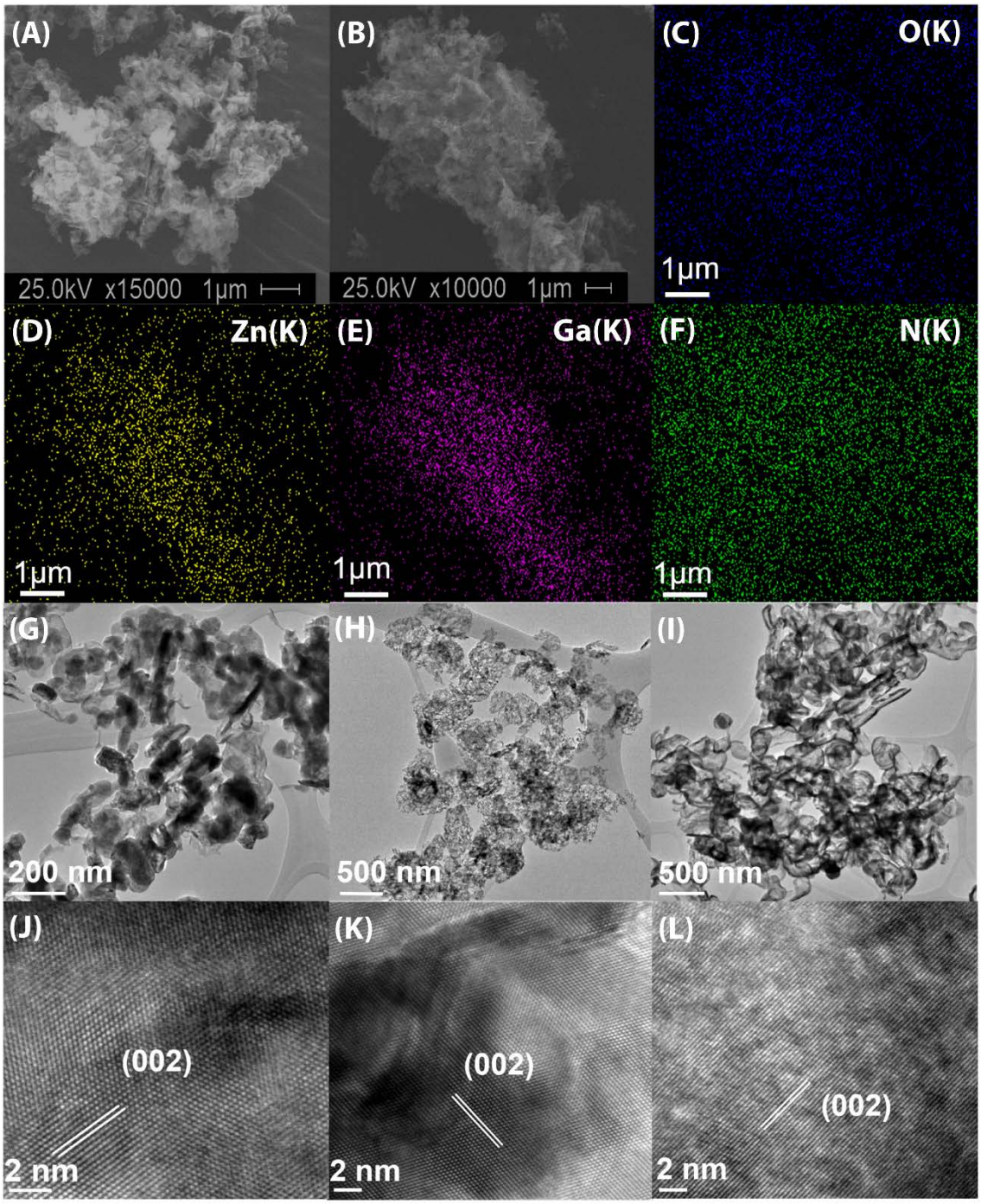

Fig. 2 | Microscopic investigation of LDH and Oxynitrides. A-B, Scanning electron micrographs of Zn-rich oxynitride (3-20) sample. **C-F,** Mapping of the constituent elements (O, Zn, Ga, N) of the sample via EDAX. **G-I,** Transmission electron micrographs of different oxynitrides (1-20, 2-20, 3-20 respectively) after 20 min of nitriding. **J-L,** High resolution TEM images of the oxynitrides (1-20, 2-20, 3-20 respectively) revealing the (002) crystal facets.

The concentrations of the cations and anions for all these oxynitrides are reported in Fig. 3A-B. Synchronous with the Zn volatilization phenomenon with increased nitriding time, we observed a decline of Zn/Ga ratio for all the samples (Fig. 3A). Although Zn volatilization results in substantial loss of Zn, samples obtained from a Zn-rich precursor (3:1) demonstrated high Zn:Ga ratios (more than 0.3). The incorporation of N via nitriding, is well depicted in the Fig. 3B, where the O:N ratio decreases with nitriding time. The major drop of O:N ratio only from 10 to 20 min suggests that 30 min of nitriding is not necessary for these samples as it results in more and more of Zn-deficient phases, without much additional N incorporation. This evolution of elemental composition is also consistent with the XRD trends where a major Zn volatilization leads to the shrinking of the cell size of Zn:Ga =1:1 sample. Zinc volatilization and nitrogen incorporation in the lattice of these oxynitrides during nitriding are depicted vividly in Fig. S1. Optimizing nitriding time (20 minutes in this case) is a key parameter as it reduces Zn volatilization. This decreased Zn content and compressive strain induced due to cell collapse reflects in the increased band gap for Zn:Ga = 1:1 sample (Fig. 3C). However for the other samples (2:1 and 3:1), although Zn volatilization occurred (as observed in Fig. 3A), we did not observe similar lattice collapse (Fig. 1D-E). Reduced Zn content is an indicator for increased band gap, however, non-collapsing crystal cell is an indication of vacancy defects being generated and tensile strain being induced. The later effects are factors of band gap reduction. Because of these two contesting processes, we observe a mixed response on band gap evolution of the 2:1 and 3:1 samples (Fig. 3C). On the whole, we demonstrate decreasing band gap with increased Zn content, a crucial route for material property tuning in these Zn oxynitrides.

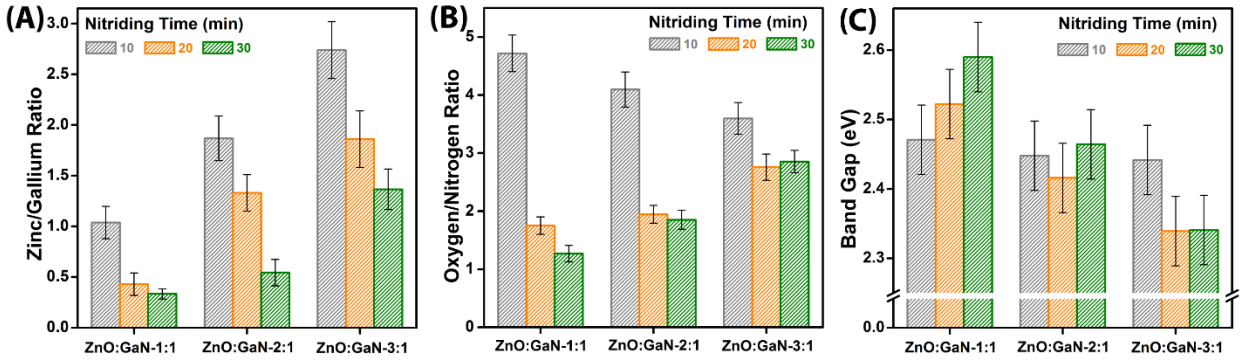

Fig. 3 | Elemental composition and band gap modulation. A-B, Variation of cation ratios (Zn^{2+}/Ga^{3+}) and anion ratios (O^{2-}/N^{3-}) in oxynitride samples with increasing nitriding time. **C,** Band gap modulation of these samples via nitriding.

The effect of composition and strain was further theoretically studied via density functional theory-based calculations. Since, probing solid solution structure is computationally expensive, as well as an exact structural configuration is also unambiguous, we investigated the vertical stacks of Zn-Ga oxynitrides (Fig. 4A). This provides the opportunity to systematically study the composition variation, and also allows for understanding the electronic states at the oxide-nitride interface. Moreover, LDH structures are vertically stacked and a controlled synthesis of oxynitrides could result in alternating layers of oxides and nitrides being formed along the *c* axis. The band gap variation with composition is clearly depicted in Fig. 4B. While PBE exchange-correlation is known to underestimate the bandgaps, hybrid functionals such as HSE06 and GW are better predictors of the bandgap[29]. For all the three methods, we observe a consistent decreasing band gap trend with increasing Zn concentration. The VBE of these oxynitrides are mostly dominated by the Zn-*3d*, N-*2p* and O-*2p* orbitals[21, 22]. Thus, higher nitride concentration (or lower Zn content) predicts higher Zn-*3d* and N-*2p* orbital repulsion at the VBE, thereby accounting for the decreased band gap. This is similar to our experimental trends as well. The effect of lattice strain, a major parameter in these materials, is portrayed in Fig. 4C. Lattice strain in these materials can be vertical or biaxial. Since the vertical heterojunction exhibits the oxide-nitride interface

along the *c* axis, we observe greater effects for vertical lattice strain. Tensile strain (or lattice expansion) is marked by positive strain, while compressive (or lattice shrinking) is denoted by negative strain. Irrespective of the material composition, we find that compressive strain causes increased band gap and tensile strain causes decreased band gap. This is due to the bonding and antibonding orbitals being stabilized and destabilized, respectively, under compression. The antibonding states at the conduction band edge (CBE) are reported to be more perturbed by this variation, resulting in net increase and decrease of band gap under compression and tension, respectively[30]. Experimentally, the compressive strain induced due to the lattice collapse in Zn:Ga=1:1 samples along with loss of Zn (Figs. 1D-E and 3A) explains the increased band gap trend (Fig.3C). Similarly, Zn loss for 2:1 and 3:1 samples (Fig. 3A) predicts band gap increase, while the tensile strain (Figs. 1D-E) induced in these samples portends reduction of band gap. These contradictory influences in 2:1 and 3:1 samples are the reasons for observed band gap fluctuation. The effect of this lattice strain, on the interface atoms are explicitly presented in Figs. 4(D-E). Along the VBE, the Zn-*3d* orbitals are aligned to $E-E_F = 0$. The resulting shift in the gap is thus evident on the CBE. The orbitals are shifted to higher energy levels at the CBE under compression, with the vertical strain (Fig. 4E) being more effective than the biaxial one (Fig. 4D).

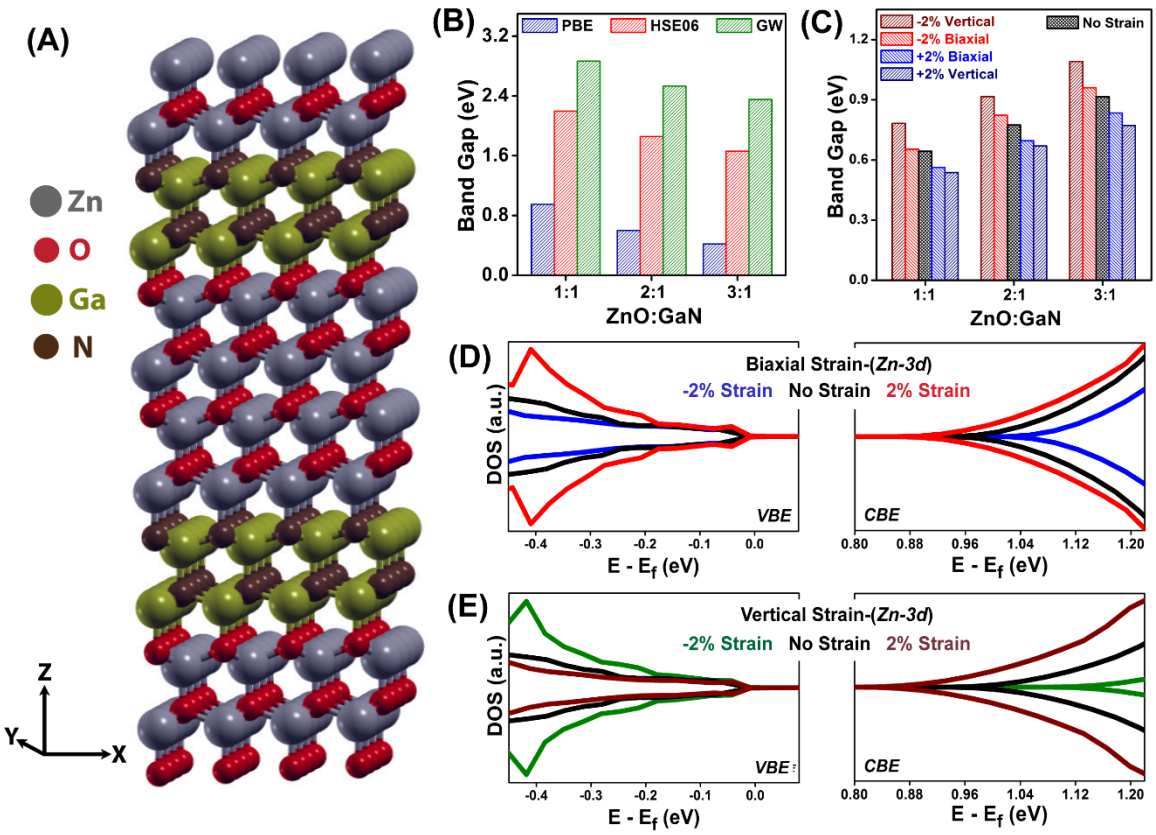

Fig. 4 | Composition and lattice strain sensitivity of the oxynitrides. A, Schematic of a vertically stacked oxynitride heterostructure. **B,** Electronic band gap variation as a function of heterostructure composition. **C,** Lattice strain induced band gap tuning of the oxynitride heterostructures. **D-E,** Variation of the atom projected density of states for Zn-*3d* orbital along the valence band and conduction band edges under biaxial and vertical lattice strain respectively.

The nitriding process of oxynitride synthesis from these LDHs is closely associated with Zn volatilization, lattice strain and introduction of vacancy defects. The resulting effects on elemental composition and bonding at the catalyst surface was probed via XPS. Fig. 5A depicts the change in the Zn-$2p_{3/2}$ peak for Zn:Ga=2:1 sample with varying nitriding time. Zn-$2p_{3/2}$ peaks in all of these samples are shifted to lower binding energy (B.E.) than that for pure ZnO samples (~1022.2 eV)[18, 31], due to the bond polarity variations of Zn-O and Zn-N. With increasing nitriding time, less surface Zn is available which is clearly rendered in the decreased peak intensities. A slight shift towards higher binding energy marks reduced presence of Zn-N bonds as more Zn is

leaves the crystal with increased nitriding. Increased Zn content (Fig. 5B) allows for higher probability of N interaction, causing a minor shift to lower B.E. For Ga-*3d* peak, there is a consistent shift to higher B.E. with increasing nitriding time (Fig. 5C). This marks the formation of Ga-O bonds due to more and more Zn volatilization[32, 33]. Fig. 5D reveals the shift of Ga-*3d* peak to lower binding energies with increased Zn composition. Higher Zn content in the sample allows for replenishment of surface Zn. Thus, the chances of Ga-O bond formation at the surface are lower with Zn-rich samples. Even the increase in Ga-*3d* peak intensities with nitriding time (Fig. 5C) and the reverse trend with increasing content (Fig. 5D) is concomitant with the above explanation. The N-*1s* peak is a reflection of the presence of Ga-N (N-*1s* spectrum for pure GaN detailed in Fig. S2) and Zn-N bonds. As reported in literature[34, 35], presence of Zn-N bonds causes low B.E. shifts, as explicitly observed in Fig. 5F. The decreased peak intensity also marks lower nitride phases at the surface, in close corroboration with higher ZnO composition. Increased nitride phase formation with time is explicit from Fig. 5E. Shift of the N-1s peak to higher B.E. is an indication of prominence of Ga-N bonds, as surface Zn content is reduced due to volatilization.

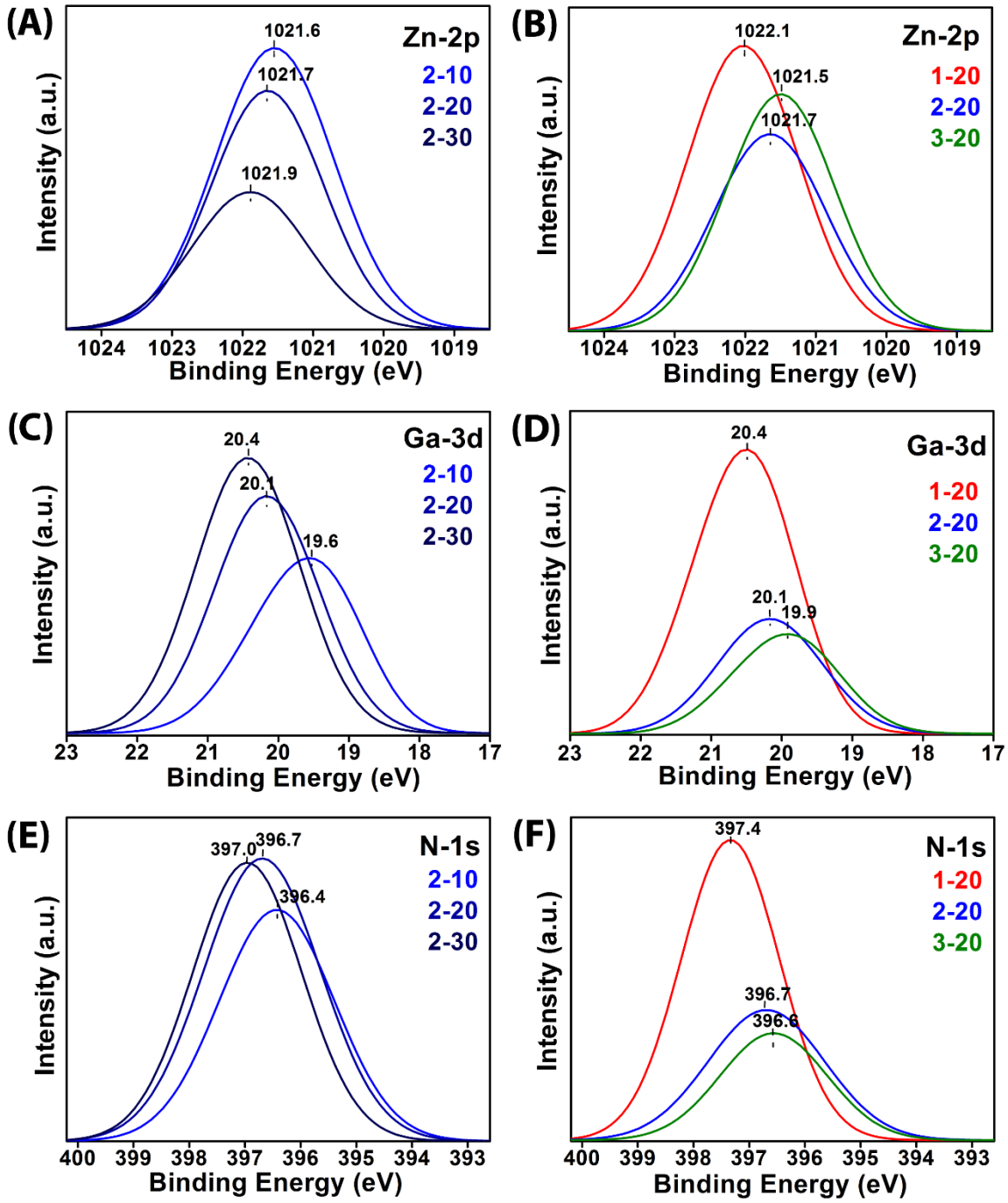

Fig. 5 | XPS based surface characterization of the oxynitrides. A-B, Zn-*2p* spectra **C-D,** Ga-*3d* spectra. **E-F,** N-*1s* spectra respectively under varying nitriding time and original precursor composition.

The XPS analyses of the O-*1s* peak also provides critical insights of the material development process via this synthesis protocol. O-*1s* peak (Fig. 6A) for pure ZnO and GaN is

essentially a combination of oxide ion and surface chemisorbed hydroxyls[33]. For the oxynitride samples, O-*1s* peak can have contributions from Zn-O, Ga-O bonds, along with surface hydroxyls and oxygen vacancy defects[36]. For the O-*1s* peak of 1-10 sample (Fig. 6B), there is an explicit presence of the oxide ion peak from ZnO and another peak that may be attributed to Ga-O bond and/or chemisorbed surface hydroxyls[18, 33]. With nitriding time, the shift of the O-*1s* peak to higher B.E. (Fig. 6C) portrays higher presence of Ga-O peaks. The minor shift of the O-*1s* peak to higher B.E. even at higher Zn content may be attributed to presence of vacant states[36] (Fig. 6D).

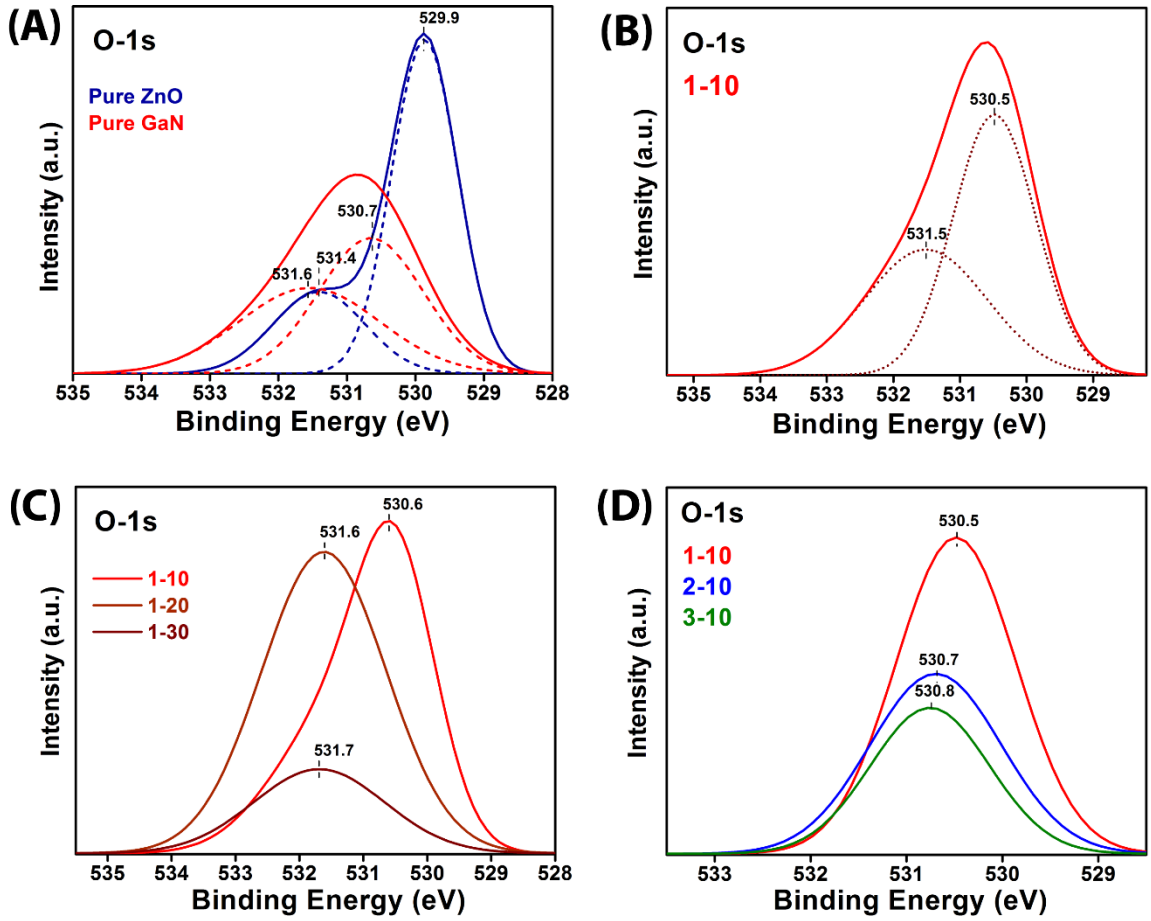

Fig. 6 | XPS based investigation of surface oxygen content. A, Surface oxygen characterization for pure ZnO and GaN samples. **B,** O-*1s* spectrum of 1-10 sample. **C-D,** O-*1s* spectra under varying nitriding time and original precursor composition.

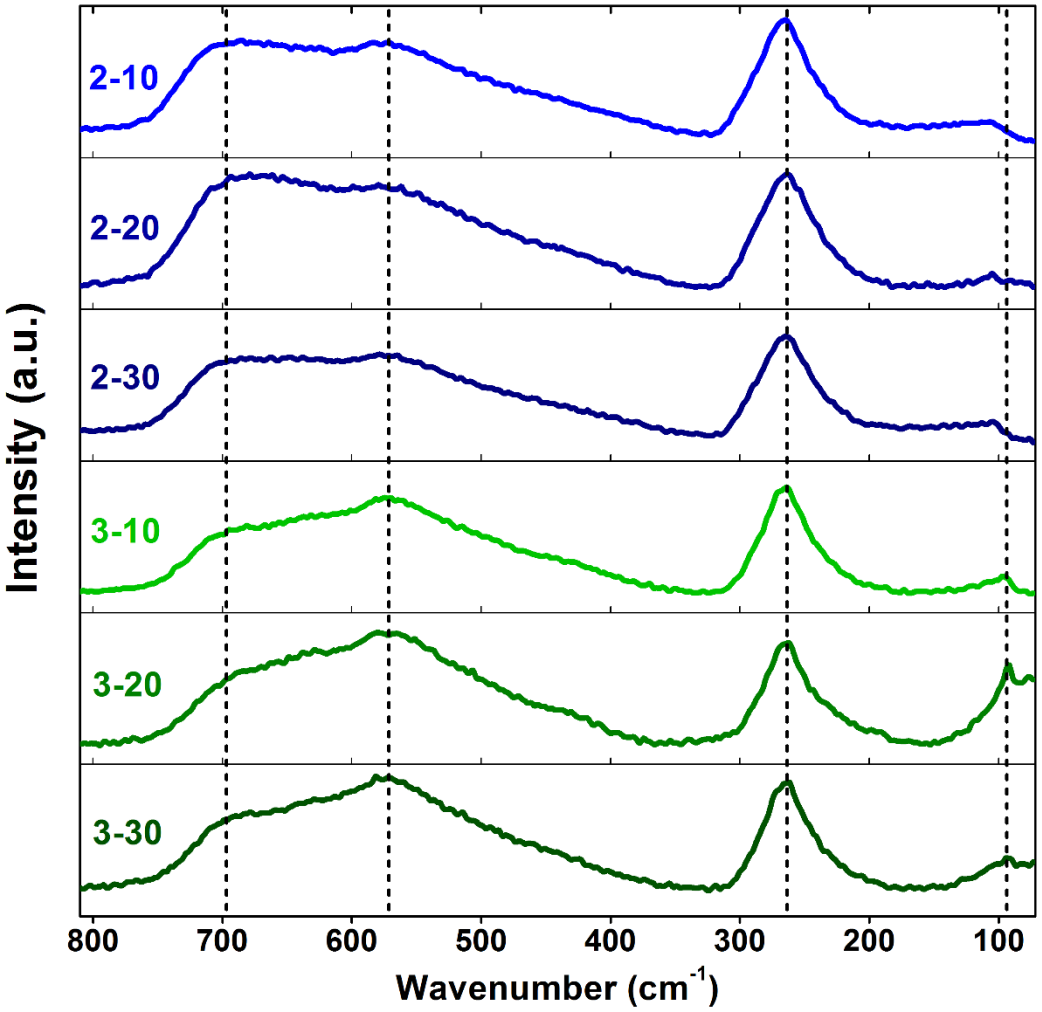

Fig. 7 | Vibrational properties. Phonon frequencies obtained in the as-synthesized oxynitrides.

Raman spectra were collected for the 2:1 and 3:1 Zn:Ga nitrided samples (Fig. 7). The peaks are largely unresolved from 500 to 700 cm^{-1}. The peaks located at ~690 and ~580 cm^{-1} are likely associated with the GaN A_1 (LO) and GaN E_2 (high) phonon, respectively[37]. A 574 cm^{-1} peak may also correspond to the ZnO 1(LO) phonon peak, associated with the A1 (LO) phonon, on the c-axis of wurtzite ZnO, which is why the peak has stronger definition in the 3-10 to 3-30 samples. When ZnO is arranged in a perpendicular arrangement, the E1 (LO) phonon[38] can be observed at 583 cm^{-1}. This implied that the shift and broad range are possibly due to the shared

phase with the GaN, but also optical phonon confinement, defect or impurity in the nanocrystal. The peaks at ~260 and ~95 cm^{-1} revealed that stress and strain are present in the heterostructures. The 260 cm^{-1} broadening occurs with decreasing Zn content and the 95 cm^{-1} relaxes.

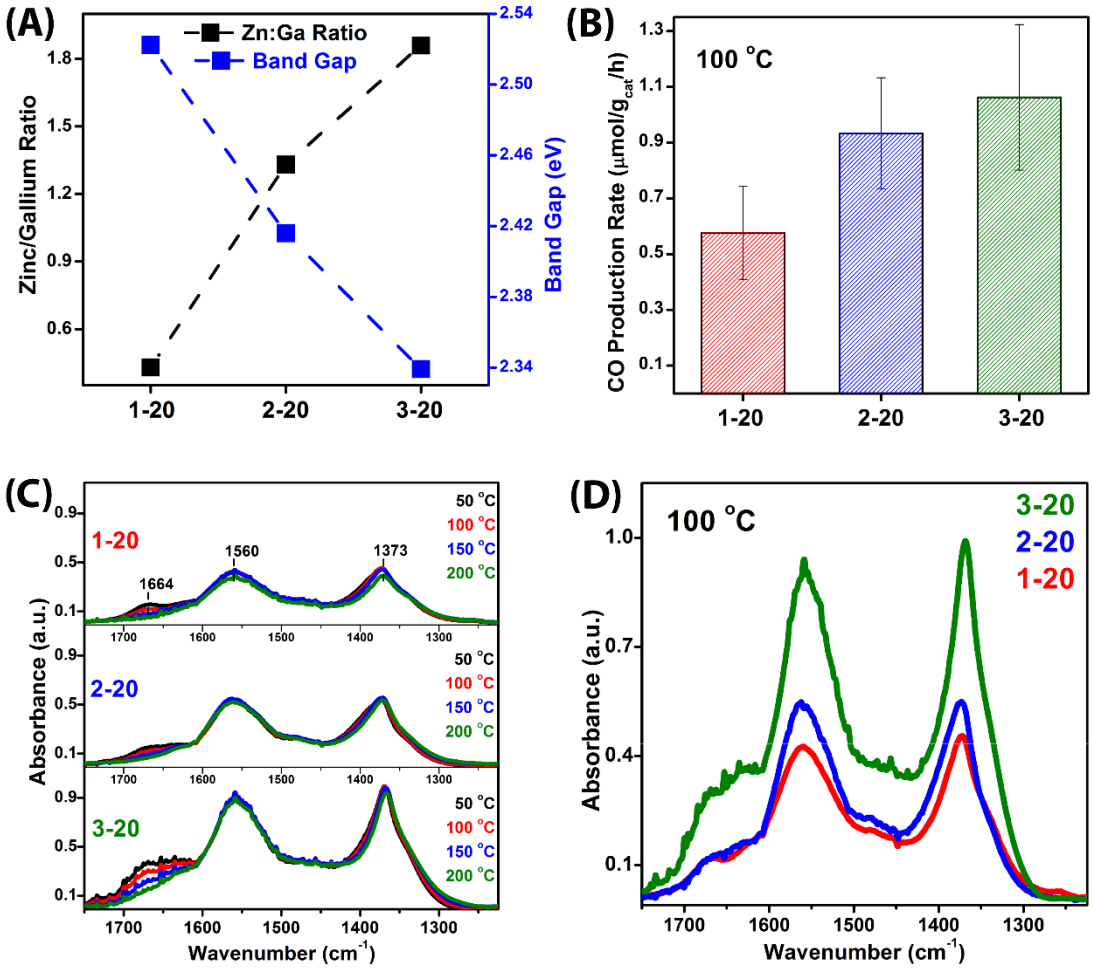

Fig. 8 | Catalytic activity. A, Band gap of the oxynitrides with varying Zn/Ga ratio. **B,** Enhanced CO production rate by increasing the Zn:Ga composition ratio in the oxynitrides. **C,** DRIFTS studies of CO_2 desorption at different temperatures. **D,** CO_2 adsorption on the oxynitrides at 100 °C.

Through this process of oxynitride synthesis, we could achieve material property tuning via intrinsically induced strain, vacancy and composition variation. Achieving high Zn content in these oxynitrides resulted in lowering of the band gap (Fig. 8A) showing promise for visible light

activity. The materials were tested for photocatalytic CO_2 reduction in a stainless steel reactor under simulated solar light. For the first time, CO_2 photoreduction was achieved over these oxynitrides without any noble metal co-catalyst. Increased CO production over Zn-rich materials (Fig. 8B) is coherent with the decreased band gap (Fig. 8A). These materials performed even better than the traditional P25 catalyst (0.41 μmol/g-catalyst/h). The surface activity of these materials was probed via CO_2 desorption studies using DRIFTS. The CO_2 adsorption over these materials in presence of water is an indication of their reactivity. Theoretically, CO_2 adsorption energies have been highlighted as a model descriptor for the catalyst reactivity[39]. Hereby, we demonstrate strong CO_2 adsorption over all the three samples at different temperatures, ranging from 50 °C to 200 °C (Fig. 8C). The major peaks are identified as bicarbonates or carboxylates (~1663 cm^{-1})[40] and carbonates (~1560 cm^{-1})[41]. Symmetrical stretching of the O-C-O bonds was also observed (~1373 cm^{-1})[42]. Explicit comparison of the three samples at 100 °C, reveals increasing CO_2 adsorption with increasing Zn content in the sample (Fig.8D), which directly matches with the photoreduction capability of these materials (Fig. 8B). Higher presence of oxygen vacancies over Zn-rich samples (Fig. 6D), along with Zn being more electropositive than Ga, provides justification for the increased CO_2 adsorption properties over 3-20 sample. The long-term stability of these materials under different ambient conditions is evident from in-situ XRD patterns (Fig. S3) and x-ray photoelectron spectra (Fig. S4) of samples irradiation with UV light (F15T8 bulbs at 75 W/m^2) for up to 3 days, thus presenting these materials as strong candidates for large scale commercial application.

CONCLUSIONS:

Through detailed analysis of the synthesis process, we were able to elucidate the modulation of band gap in these materials as a function of structure, composition, lattice strain and vacancy and their close correlation to experimental synthesis protocol. Solar photocatalytic reduction of CO_2 to CO was achieved over these materials for the first time without any expensive dopants or noble metal impregnation. We also demonstrated that the Zn-Ga materials had a Eg range from 2.33 eV to 2.59 eV which was easily tunable from varying nitriding time and cationic ratio. The highest CO production rate was 3-20 sample reaction at 100 °C, which produced 1.06 $\mu mol\text{-}g^{-1}\text{-}h^{-1}$, higher than the control TiO_2 experiments, and other reported pure TiO_2 solar photoreaction experiments. This paves the path for future research on these materials for systematic tailoring of material properties for desired photocatalytic and optical applications.

COMPETING INTERESTS:

The authors declare no competing financial interests.

ACKNOWLEDGEMENTS:

The authors acknowledge funding from the NASA Science Mission Directorate Science Innovation Fund and the NASA Space Technology Mission Directorate Center Innovation Fund. This work was also supported by the NASA Kennedy Space Center and University of South Florida Space Act Agreement. The authors acknowledge funding from NSF through grants EEC-1301054 and EEC-1560303. DM appreciates the financial support from the Office of Graduate Studies, USF through the Dissertation Completion Fellowship. The authors acknowledge USF Research Computing for high performance computing resources and help from Shawn Sasser and Bianca Dyer. The authors thank Dr. Brad Sutter at NASA, JSC for his help with the in-situ XRD

data collection. Appreciation is regarded to Dr. Paul Hintze, Philip Howard and Michael Kosiba at NASA, KSC for thoughtful discussions of experimental technique and data.

AUTHOR CONTRIBUTIONS:

A.J.M conducted most experiments, D.M and J.C performed the DFT computations, S.R. conducted the microscopy studies, and K.M synthesized the catalysts, D.M. performed the DRIFTS studies, analyzed the experimental and computational data, and drafted the manuscript. J.N.K and V.R.B provided help and suggestions throughout this project. All authors commented on and revised the manuscript.

REFERENCES:

1. P. D. Tran, L. H. Wong, J. Barber and J. S. C. Loo, *Energy & Environmental Science*, 2012, **5**, 5902-5902.
2. W. C. Chueh, C. Falter, M. Abbott, D. Scipio, P. Furler, S. M. Haile and A. Steinfeld, *Science*, 2010, **330**, 1797-1801.
3. A. H. McDaniel, E. C. Miller, D. Arifin, A. Ambrosini, E. N. Coker, R. O'Hayre, W. C. Chueh and J. Tong, *Energy & Environmental Science*, 2013, **6**, 2024-2028.
4. D. Maiti, B. J. Hare, Y. A. Daza, A. E. Ramos, J. N. Kuhn and V. R. Bhethanabotla, *Energy & Environmental Science*, 2018, **11**, 648-659.
5. Y. A. Daza, D. Maiti, R. A. Kent, V. R. Bhethanabotla and J. N. Kuhn, *Catalysis Today*, 2015, **258, 2**, 691-698.
6. K. Li, X. An, K. H. Park, M. Khraisheh and J. Tang, *Catalysis Today*, 2014, **224**, 3-12.
7. K. Maeda and K. Domen, *Bulletin of the Chemical Society of Japan*, 2016, **89**, 627-648.
8. N. Zhang, S. Ouyang, T. Kako and J. Ye, *Chemical Communications*, 2012, **48**, 1269-1271.
9. A. Goeppert, M. Czaun, J.-P. Jones, G. K. Surya Prakash and G. A. Olah, *Chemical Society Reviews*, 2014, **43**, 7995-8048.
10. B. Ohtani, *Physical Chemistry Chemical Physics*, 2014, **16**, 1788-1797.
11. L. Mohapatra and K. Parida, *Journal of Materials Chemistry A*, 2016, **4**, 10744-10766.
12. Y. Zhao, X. Jia, I. N. Waterhouse Geoffrey, L. Z. Wu, C. H. Tung, D. O'Hare and T. Zhang, *Adv. Energy Mater.*, 2016, **6**, 1501974.
13. N. Ahmed, Y. Shibata, T. Taniguchi and Y. Izumi, *Journal of Catalysis*, 2011, **279**, 123-135.
14. Y. Izumi, *Coordination Chemistry Reviews*, 2013, **257**, 171-186.
15. Q. Liu, M. Xu, B. Zhou, R. Liu, F. Tao and G. Mao, *European Journal of Inorganic Chemistry*, 2017, **2017**, 2195-2200.

16. K. Maeda, K. Teramura, D. Lu, T. Takata, N. Saito, Y. Inoue and K. Domen, *Nature*, 2006, **440**, 295.
17. K. Maeda and K. Domen, *The Journal of Physical Chemistry C*, 2007, **111**, 7851-7861.
18. K. Maeda, K. Teramura, T. Takata, M. Hara, N. Saito, K. Toda, Y. Inoue, H. Kobayashi and K. Domen, *The Journal of Physical Chemistry B*, 2005, **109**, 20504-20510.
19. Y. Lee, H. Terashima, Y. Shimodaira, K. Teramura, M. Hara, H. Kobayashi, K. Domen and M. Yashima, *The Journal of Physical Chemistry C*, 2007, **111**, 1042-1048.
20. S. Yan, H. Yu, N. Wang, Z. Li and Z. Zou, *Chemical Communications*, 2012, **48**, 1048-1050.
21. S. H. Wei and A. Zunger, *Physical Review B*, 1988, **37**, 8958-8981.
22. K. Maeda and K. Domen, *Chemistry of Materials*, 2010, **22**, 612-623.
23. J. Su, Y. Wei and L. Vayssieres, *The Journal of Physical Chemistry Letters*, 2017, **8**, 5228-5238.
24. D. Voiry, H. S. Shin, K. P. Loh and M. Chhowalla, *Nature Reviews Chemistry*, 2018, **2**, 0105.
25. D. P. Chen and S. E. Skrabalak, *Inorganic Chemistry*, 2016, **55**, 3822-3828.
26. Y.-L. Hu, S. Ou, J. Huang, H. Ji, S. Xiang, Y. Zhu, Z. Chen, C. Gong, L. Sun, J. Lian, D. Sun, Y. Fu and T. Ma, *Inorganic Chemistry*, 2018, **57**, 9412-9424.
27. D. P. Chen, J. C. Neuefeind, K. M. Koczkur, D. L. Bish and S. E. Skrabalak, *Chemistry of Materials*, 2017, **29**, 6525-6535.
28. J. Wang, B. Huang, Z. Wang, P. Wang, H. Cheng, Z. Zheng, X. Qin, X. Zhang, Y. Dai and M.-H. Whangbo, *Journal of Materials Chemistry*, 2011, **21**, 4562-4567.
29. D. Maiti, J. Cairns, J. N. Kuhn and V. R. Bhethanabotla, *The Journal of Physical Chemistry C*, 2018, **122**, 22504-22511.
30. S. K. Yadav, T. Sadowski and R. Ramprasad, *Physical Review B*, 2010, **81**, 144120.
31. A. Sahai and N. Goswami, *AIP Conference Proceedings*, 2015, **1665**, 050023.
32. M. Kumar, S. K. Pasha, T. C. Shibin Krishna, A. P. Singh, P. Kumar, B. K. Gupta and G. Gupta, *Dalton Transactions*, 2014, **43**, 11855-11861.
33. E. A. Alam, I. Cortés, M. P. Besland, A. Goullet, L. Lajaunie, P. Regreny, Y. Cordier, J. Brault, A. Cazarré, K. Isoird, G. Sarrabayrouse and F. Morancho, *Journal of Applied Physics*, 2011, **109**, 084511.
34. M. Futsuhara, K. Yoshioka and O. Takai, *Thin Solid Films*, 1998, **322**, 274-281.
35. M. Dinescu, P. Verardi, C. Boulmer-Leborgne, C. Gerardi, L. Mirenghi and V. Sandu, *Applied Surface Science*, 1998, **127-129**, 559-563.
36. H.-B. Fan, S.-Y. Yang, P.-F. Zhang, H.-Y. Wei, X.-L. Liu, C.-M. Jiao, Q.-S. Zhu, Y.-H. Chen and Z.-G. Wang, *Chinese Physics Letters*, 2007, **24**, 2108.
37. T. C. Shibin Krishna, N. Aggarwal, G. A. Reddy, P. Dugar, M. Mishra, L. Goswami, N. Dilawar, M. Kumar, K. K. Maurya and G. Gupta, *RSC Advances*, 2015, **5**, 73261-73267.
38. R. Zhang, P.-G. Yin, N. Wang and L. Guo, *Solid State Sciences*, 2009, **11**, 865-869.
39. D. Maiti, Y. A. Daza, M. M. Yung, J. N. Kuhn and V. R. Bhethanabotla, *Journal of Materials Chemistry A*, 2016, **4**, 5137-5148.
40. C.-C. Yang, Y.-H. Yu, B. van der Linden, J. C. S. Wu and G. Mul, *Journal of the American Chemical Society*, 2010, **132**, 8398-8406.
41. G. Jacobs, L. Williams, U. Graham, D. Sparks and B. H. Davis, *The Journal of Physical Chemistry B*, 2003, **107**, 10398-10404.

42. N. H. Elsayed, D. Maiti, B. Joseph and J. N. Kuhn, *Catalysis Letters*, 2018, **148**, 1003-1013.